

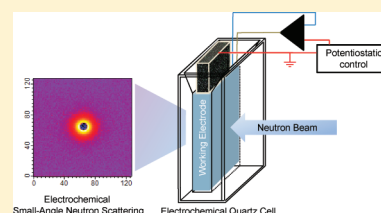
# In situ Electrochemical Small-Angle Neutron Scattering (eSANS) for Quantitative Structure and Redox Properties of Nanoparticles

Vivek M. Prabhu\*<sup>†</sup> and Vytas Reipa<sup>‡</sup><sup>†</sup>Polymers Division and <sup>‡</sup>Biochemical Science Division, Material Measurement Laboratory, National Institute of Standards and Technology (NIST), Gaithersburg, Maryland 20899, United States

## Supporting Information

**ABSTRACT:** The rapid growth in nanomaterial applications have revealed limitations in available physicochemical characterization methods. An in situ electrochemical small-angle neutron scattering (eSANS) methodology was devised that enables direct measurements of nanomaterial dispersion structure while undergoing reduction–oxidation (redox) reactions at the vitreous carbon electrode. Furthermore, these porous electrodes are amenable to contrast-variant neutron scattering strategies to measure nanoparticle structure and polymer conformation in multicomponent systems. The eSANS method was tested for feasibility by characterizing ZnO nanoparticles in 50 mmol/L NaCl deuterium oxide solution undergoing bulk electrolysis at negative potentials. Irreversible nanoparticle structural changes are observed during the potential cycle. The complete reduction of Zn<sup>2+</sup> to Zn<sup>0</sup> nanoparticles is unlikely, but a peak in the characteristic correlation length occurs during the redox bias with reduced average characteristic size.

**SECTION:** Nanoparticles and Nanostructures



The demand for engineered nanomaterials in growing research sectors, such as energy, cosmetics, and healthcare products, requires materials with widely disparate physicochemical properties. The redox properties of nanomaterials are crucial to certain applications such as photocatalytic materials and matching semiconductor band gaps for photovoltaic devices. However, the redox properties are also important to nanomaterial toxicology<sup>1</sup> because they may interact with biological charge transfer pathways or induce oxidative stress by generating reactive-oxygen species.<sup>2–4</sup> With particle sizes approaching the quantum confinement range and conjugation to organic ligands (e.g., to stabilize dispersions for magnetic resonance imaging), their redox properties are governed by the position of the electronic band edges<sup>5</sup> and may differ from the tabulated thermodynamic properties of parent bulk materials. Spectroscopic in situ analysis of species undergoing redox reaction (spectroelectrochemistry) quantifies electron transfer and energetics of the reaction via potential control.<sup>6</sup> Optical spectroscopies (ultraviolet–visible, infrared absorbance, fluorescence, Raman) are by far the most common analytical techniques employed for this purpose. However, electron paramagnetic resonance, nuclear magnetic resonance, and X-ray absorbance spectroscopies have also been reported.<sup>7</sup> Here we demonstrate the potential of in situ electrochemical small-angle neutron scattering (eSANS) measurements on ZnO nanoparticles undergoing electrolysis under potentiostatic condition at an inert electrode. Many direct routes are available to probe redox properties, such as scanning probe methods,<sup>8</sup> even in situ electron microscopy in fluidic channels.<sup>9</sup> However, scattering methods (X-ray and neutron) provide unique capabilities to probe transformational kinetics with widely disparate materials such as organics and inorganics, including core–shell metal

nanoparticles<sup>10</sup> with variable sensitivity at the nanoscale. A transmission SANS measurement was demonstrated for electrochemical dealloying under potential control,<sup>11</sup> illustrating the strengths of scattering methods to probe structure.

SANS was performed at the NIST Center for Neutron Research with cold neutrons of 6.0 Å wavelength ( $\lambda$ ) with spread ( $\Delta\lambda/\lambda$ ) of 0.115. The scattered intensity  $I(Q)$  was measured as a function of the wave vector ( $Q$ ) defined by  $Q = (4\pi/\lambda) \sin(\theta/2)$ , where  $\theta$  is the scattering angle. Three sample-to-detector distances were used: 13, 4, and 1 m that provide  $0.00335 \text{ \AA}^{-1} \leq Q \leq 0.542 \text{ \AA}^{-1}$ . Data were placed on an absolute intensity scale via direct beam flux measurement, detector sensitivity and element size, transmission, sample-to-detector distance, and sample scattering volume considerations. Details regarding data collection and reduction can be found elsewhere.<sup>12</sup> The eSANS working electrode was 80 pores per inch ( $\sim 300 \mu\text{m}$  radius macropores) reticulated vitreous carbon (Electrosynthesis, Inc.) cut to dimensions 3.8 cm  $\times$  1.2 cm  $\times$  0.4 cm and fit within the center of a 4 mm path quartz spectroscopic cuvette (Starna), a Ag/AgCl in 3 mol/L KCl reference electrode, and platinum wire coil counter electrode, separated from the working electrode by dialysis tubing under potentiostat control (Omni 90). All experiments were performed at  $25.0 \pm 0.1 \text{ }^\circ\text{C}$  to minimize variability. Aqueous dispersions of average 35 nm hydrodynamic radius ZnO nanoparticles (Aldrich) were lyophilized to remove H<sub>2</sub>O and dispersed as 0.1% by volume ZnO particles in 50 mmol/L NaCl in D<sub>2</sub>O and 0.22  $\mu\text{m}$  filtered into eSANS cells. The samples are

Received: January 31, 2012

Accepted: February 16, 2012

Published: February 16, 2012

stable for more than one day, after which sedimentation appears. Therefore, in the presence of salt this system has limited long-term stability. Experiments were conducted in the dark, thus eliminating the possibility of the photochemical reactions.<sup>5,13</sup> Uncertainties are estimated by one standard deviation of the mean. Fits of the eSANS data are made by a weighted least-squares minimization, and error bars correspond to one standard deviation. Limits are left out for clarity when smaller than the plotted symbols.

The scattering properties of the carbon electrodes are critical to this approach because they are in the direct neutron beam path (Figure 1, inset). SANS from dry vitreous carbon,

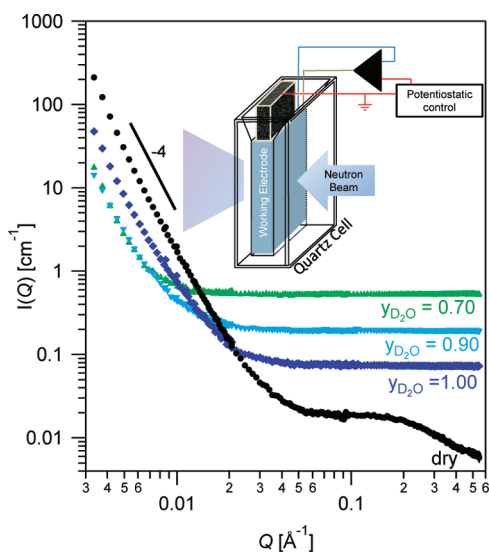


**Figure 1.** SANS of dry vitreous carbon and in three different volume fraction ( $y$ ) of  $D_2O$  in  $D_2O:H_2O$  isotopic mixtures. Inset shows a schematic of the transmission eSANS quartz cell with working electrode under potentiostatic control.

mounted in the quartz cell is isotropic and azimuthally averaged, leading to the scattering profile shown in Figure 1. Two features are observed: a low- $Q$  power law ( $Q^{-4}$ ) and decay in the high- $Q$  region. The structural properties of vitreous carbon are directly related to the thermal processing of precursor organics to form the conductive carbon. Gupta and Harrison used small-angle X-ray scattering (SAXS) to study the effects of processing temperature on carbonized phenolic resins that are precursors to vitreous carbon.<sup>14,15</sup> They found that during the thermal-processing treatment nanopores are formed via cross-linking reaction of the phenolic resin; these nanopores have structure and may show positional order, leading to a broad scattered intensity peak. Higher processing temperatures cause nanopores to coalesce, increasing the average pore size and eventually microporosity within the vitreous carbon. The scattering from this hierarchical structure of micro- and nanopores is consistent with the SANS data shown in Figure 1. The decay at high- $Q$  in Figure 1 is consistent with a form factor scattering by nanopores, whereas the power law scattering in the low- $Q$  that plateaus is the Porod region for scattering by the large interfacial area from micropores. The scattering of the dry vitreous carbon at  $Q > 0.15 \text{ \AA}^{-1}$  was initially analyzed by the Debye–Bueche model<sup>16</sup> (Supporting Information (SI)), leading to a correlation length of 0.23 nm that is smaller than the distance between graphitic planes (0.36 nm). SAXS on the same sample led to a correlation length of

0.30 nm. Whereas the high- $Q$  data may be analyzed within the Debye–Bueche model, it does not appear to characterize nanopore dimensions, considering that the position of the high- $Q$  decay implies larger characteristic size.

To quantify the nano- and microporosity, we fit the dry vitreous carbon data in Figure 1 to a combined Porod law and Schulz-distribution of spheres.<sup>12</sup> For neutron scattering, the difference in scattering length density ( $b_v$ ) is the source of contrast quantified by  $b/v$ , where  $b$  is the total coherent scattering length within molar volume,  $v$ . From this minimal modeling, the medium was air ( $b_{v,\text{air}} = 0$ ), and vitreous carbon  $b_v$  was fixed to  $4.57 \times 10^{-6} \text{ \AA}^{-2}$  to minimize the number of parameters and fit the average pore radius ( $R$ ), polydispersity index ( $z$ ), nanopore volume fraction ( $\phi$ ),  $Q$ -independent background ( $I_{\text{back}}$ ), and Porod constant  $K_p = 2\pi S_V^d (b_{v,\text{carbon}} - b_{v,\text{air}})^2$  that provides the surface area to volume ratio ( $S_V^d$ ). Using this approach, the average nanopore radius was  $6.02 \pm 0.01 \text{ \AA}$ ,  $z = 0.19$ , and  $\phi = 0.00516 \pm 0.00003$ . Therefore, the fraction of nanopores is low, consistent with the scattering with no inter-pore correlations that would give rise to a peak, and the size is much smaller than the nanoparticles. The Porod constant provides  $S_V^d$  but not the size of the micropores. Because the experimental data do not plateau into the low- $Q$  (no Guinier region), it is not possible to extract an accurate micropore size without assumption. However, an estimate of the minimum size was performed by fitting to a bimodal Schulz-distribution of spheres that led to a characteristic radius greater than  $6 \mu\text{m}$ , assuming a fixed polydispersity index at 0.2 and pore volume fraction of 0.03 estimated gravimetrically. Micropores smaller than  $6 \mu\text{m}$  shift the model scattering to high- $Q$ , inconsistent with the experimental data. Therefore, the nano- and micropores within the vitreous carbon fibers are well-separated in size from the nanoparticles. The 35 nm nanoparticles are able to probe the high-surface-area electrode and are essentially excluded from the nanopores but able to access the micropores. If the pores were closed, then their scattering contrast would dominate over dispersed particles. However, if the nanopores were open and solvent accessible, then the solvent contrast could be matched to the vitreous carbon to reduce the macro- and nanopore contribution to the total scattering.

Upon the addition of  $D_2O$  to the eSANS cell containing the vitreous carbon electrode, the high- $Q$  decay feature is substantially reduced (Figure 1) in contrast. The characteristic decay contributes to the signal but only just above the scattering at the level of the solvent background (SI). Furthermore, the  $Q^{-4}$  scaling remains, but with lower scattered intensity. The reduced scattering must be caused by a change in contrast. If the origin of scattering in the low- $Q$  region was only closed pores, then no change would be expected because the contrast between carbon and air-filled pore would be constant. The air must be displaced by  $D_2O$  that wets the electrode, therefore reducing the contrast but preserving the  $Q$ -dependence. This remains true as the volume fraction of  $H_2O$  is increased (Figure 1), which changes the average  $b_v$  of the solvent to reach contrast match that minimizes the forward coherent scattering. The estimated contrast match point occurs at  $y_{D_2O} = 0.745$  ( $b_v = 4.57 \times 10^{-6} \text{ \AA}^{-2}$ ) with scattering not completely eliminated (SI). To better understand the pore filling the Porod law with Schulz-distribution of spheres was fit to the three different solvent data. The nanopore characteristics ( $R$ ,  $z$ ,  $\phi$ ) were fixed based on the dry analysis, and only the background and Porod prefactor were fit. The reduced

nanopore contrast due to the added solvent was sufficient to fit just above the background implying nanopore filling (SI). Insight into the fraction of filled micropores may be understood from the variability in Porod  $K_p$  prefactor. Because the scattering was not eliminated near the contrast point, a fraction of pores may not fill completely, giving rise to excess contrast. Assuming a two-state model of wet and dry interfaces, the Porod constant would have the following dependence

$$K_p = 2\pi S_V^w (b_{v,\text{carbon}} - b_{v,\text{solvent}})^2 + 2\pi S_V^d (b_{v,\text{carbon}})^2 \quad (1)$$

where  $S_V^w$  is the wet surface-to-volume ratio. A plot of the Porod prefactor as a function of the solvent-carbon contrast factor yields a straight line with finite intercept (SI), estimating that ~89% of the total surface-to-volume ratio of the vitreous carbon is wet by solvent.

The eSANS strategy was also examined with Pt wire-grid electrodes shown in Figure 2. In this case, the wire grid is

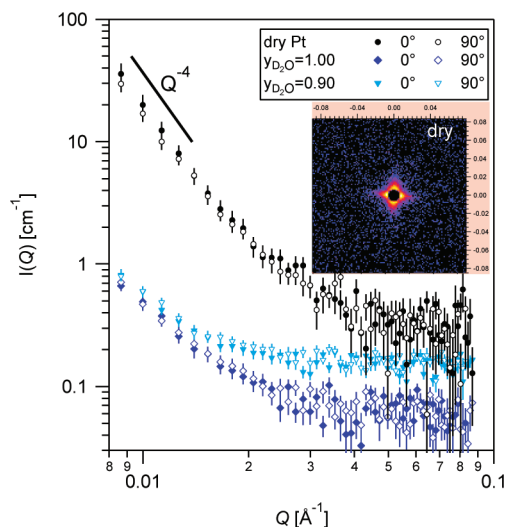


**Figure 2.** Anisotropic SANS from Pt wire-grid. Dry and two different  $D_2O$  concentrations with data averaged along vertical ( $0^\circ$ ) and horizontal pixels ( $90^\circ$ ) on the detector. Inset shows the 2-D SANS detector image for the dry Pt wire-grid.

oriented perpendicular to the incoming beam, leading to anisotropic scattering. This scattering also follows a  $Q^{-4}$  scaling. On the basis of the mass density and scattering length of Pt, the contrast match point is close to pure  $D_2O$  but not eliminated because the  $b_v$  of Pt ( $6.36 \times 10^{-6} \text{ \AA}^{-2}$ ) is slightly higher than  $D_2O$  ( $6.33 \times 10^{-6} \text{ \AA}^{-2}$ ). While it is possible to perform eSANS with these Pt wire-grids, direct exposure of Pt to high-flux neutron beams leads to activation, whereas carbon electrodes under direct beam exposure were immediately cleared following health-physics handling protocols. Furthermore, the Pt has a lower overpotential for reduction of  $H_2O$  ( $D_2O$ ), limiting the potential scan range to observe ZnO reactions.

ZnO disk-like nanoparticles were used as a test system for eSANS with the vitreous carbon electrodes. ZnO nanomaterials are important for photovoltaics as well as an efficient ultraviolet light absorber for sunscreen materials. A major concern regarding nanoparticle health and safety is the chemical stability of these particles, resulting in ZnO dissolution and  $Zn^+$  ion release that is capable of inducing biological oxidative stress pathways<sup>17,18</sup> and cell contact for a toxic response.<sup>19,20</sup>

Therefore, identification of potentially hazardous nanomaterial structural properties could allow material redesign to improve safety.<sup>21,22</sup> Unfortunately, the contrast match condition for the vitreous carbon was nearly identical to the ZnO ( $b_v \approx 4.7 \times 10^{-6} \text{ \AA}^{-2}$ ) rendering the particles nearly undetectable. Therefore, we examined ZnO scattering during the quasi-stationary linear potential scan in 50 mmol/L NaCl in  $D_2O$  and subtracted the scattering of the pure solvent in electrode blank to provide the excess scattering shown in Figure 3. This

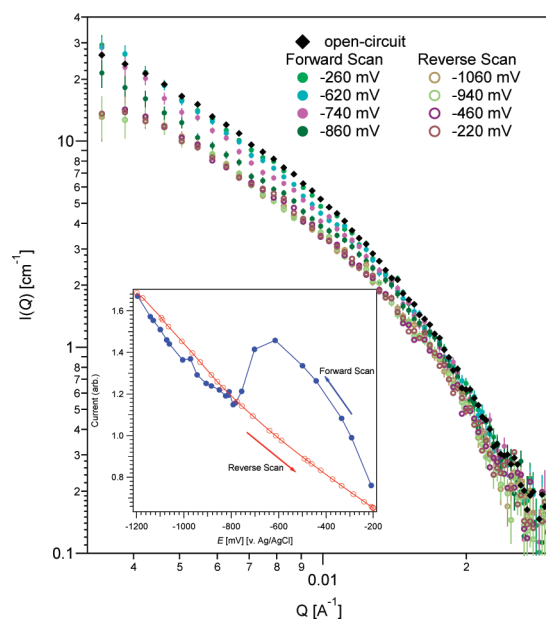


**Figure 3.** Selected eSANS data under forward and reverse potential scan with inset potentiostat current reading and controlled potential (vs Ag/AgCl).

direct subtraction yields the same scattering form as the solvent subtracted particles (SI) in the absence of potential, therefore testing the assumption of lack of specific binding to the carbon electrode. Smaller nanoparticles that scatter to higher- $Q$  above the flat electrode background would improve the method.

The forward linear scan applied was from  $-0.20$  to  $-1.2$  V (vs Ag/AgCl, 3 mol/L KCl), and reverse scan to  $-0.20$  V with a scan rate of 6 mV/min eSANS data was recorded in 20 min intervals to achieve sufficient statistics, therefore averaging over 0.120 V per scan. The potential range was not influenced by the electrolysis of water but covers an expected reduction of ZnO into Zn from bulk Pourbaix diagrams.<sup>23</sup> Selected data presented in Figure 3 show an increase in scattering coincident with the reductive current peak at approximately  $-0.60$  V, followed by a decrease in intensity across the broad  $Q$ -range and meet at high- $Q$ . The changes in scattering were analyzed within the Ornstein–Zernike (OZ) plot that provides the correlation length ( $\xi$ ) and scattered intensity at zero angle ( $I(0)$ ).

Because of the limited  $Q$ -range (13 m configuration) for the eSANS experiment, it was not possible to fit the SANS data with nanoparticle shape-dependent (form factor) primarily due to polydispersity, but the OZ analysis provides a statistical average with the understanding of an anticipated phase change or phase transition by electrochemical potential rather than more commonly in temperature or pressure. The data follow the OZ dependence as shown in Figure 4a. From this, the scattered intensity to zero angle (Figure 4b) is proportional to

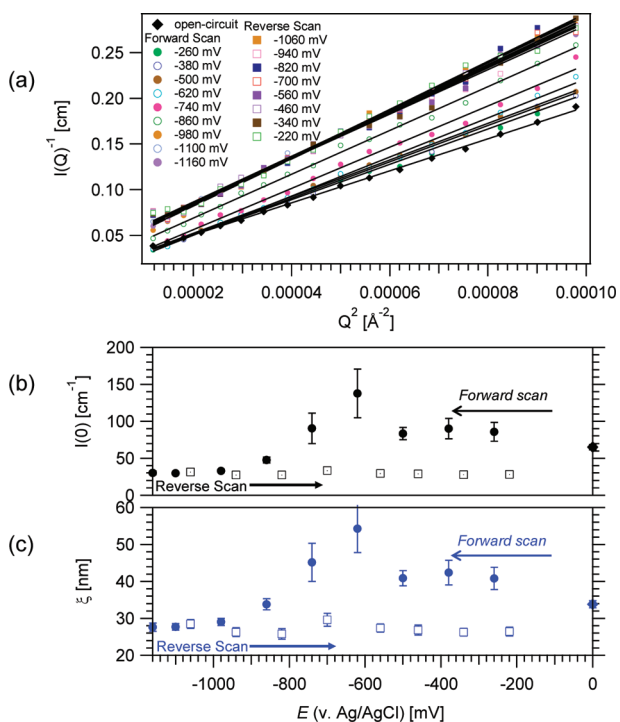


**Figure 4.** (a) OZ fits (solid lines) to nanoparticle structure under negative potential scan, (b) scattered intensity to  $Q = 0$ , and (c) correlation length from OZ plot as functions of forward (●), reverse scans (□), and open-circuit (◆) before scan. Uncertainties are one standard deviation from the mean via propagation of errors.

the contrast factor ( $(\Delta b_v)^2$ ) and amplitude of the concentration fluctuations.<sup>24</sup> The correlation length (Figure 4c) for fluctuations is also determined and plotted as a function of potential. Both parameters show an irreversible structural change with a midpoint potential of approximately  $-0.65$  V (Figure 4). The correlation length is on the scale of the particle dimensions without applied potential (open-circuit) and increases near the current maximum during the forward potential scan, followed by a gradual drop consistent with an overall particle cluster-size decrease expected by partial ZnO to Zn transition. The peak in  $\xi$  shows clustering of multiple nanoparticles takes place, illustrating that the solution structure is dependent on the redox potential. Aggregation of ZnO particles appears during plating via electrochemical reduction, causing an inhomogeneous deposition and porous structure.<sup>25</sup> Neutron scattering may follow these complex conditions in situ under conditions challenging to electron microscopy and spectroscopy. Furthermore, scattering by particles to zero angle provides,  $I(0) \approx (\Delta b_v)^2 C_{\text{NP}} V_{\text{NP}}^2$ , where  $C_{\text{NP}}$  and  $V_{\text{NP}}$  are the concentration and volume of nanoparticles, respectively. Therefore, sensitive to changes in both structure and dispersion extent. The reverse potential scan did not produce appreciable eSANS data variation as shown as  $I(0)$  and  $\xi$  plots versus  $E$ , implying an irreversible change in nanoparticle cluster size but stable dispersion.

To verify the redox eSANS scan and reductive peak, we measured ZnO nanoparticle absorbance separately as a function of applied potential using a custom thin-layer spectroelectrochemical cell<sup>6</sup> (Figure 5). An irreversible absorbance increase at 360 nm was recorded during the cathodic potential scan at  $E < -0.3$  V (Figure 5b), demonstrating a single-electron charge-transfer transition with a midpoint potential  $E_0 = -0.5$  V

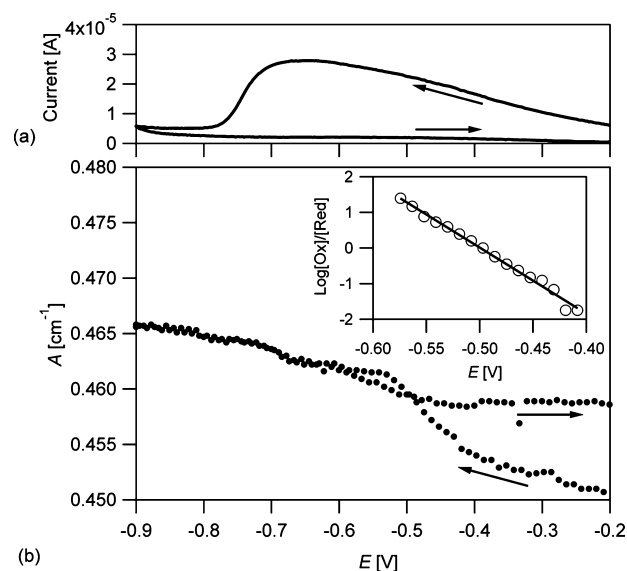


**Figure 5.** Current (a) and absorbance at 360 nm (b) traces, recorded during a potential scan at 0.1 mV/s in a thin layer spectroelectrochemical cell. Inset shows a cathodic portion of the absorbance plotted in Nernstian coordinates.

(Figure 5b, inset). This value is rather close to the reported conduction band edge<sup>26</sup> ( $-0.54$  V vs Ag/AgCl) and suggests electron injection into the conduction band or shallow trap states. Further fate of the injected electron is not known, however, it could be stored in O defect traps<sup>27</sup> or as  $\text{Zn}^+$  ions caused by the partial ZnO reduction.<sup>28</sup> Full ZnO reduction, however, is unlikely in our potential range. ( $E = -1.26$  V for  $\text{ZnO} + \text{H}_2\text{O} + 2e^- \rightarrow \text{Zn}^0 + 2\text{OH}^-$ ).

Combining SANS with electrochemical methods via porous vitreous carbon electrodes reduces an interfacial redox event into a bulk scattering method. It also allows us to monitor the redox structural changes in the dark, eliminating potential photochemical effects when conducting optical spectroelectrochemistry of light-sensitive nanoparticles such as ZnO.<sup>26</sup> The approach outlined here is extendable to contrast variant strategies. The ZnO nanoparticle studied was analyzed within the OZ plot. The independent electrochemical readout and eSANS prove that the ZnO structure is coupled to the redox state changes quantitatively. Importantly, vitreous carbon has negligible neutron absorption and incoherent scattering contributions and critically, regarding safety, do not activate under direct beam exposure to high-flux neutron sources that cannot be concluded for platinum and gold working electrodes. This opens multiple opportunities to understand redox-related structural features of dispersed nanoparticle solutions via the eSANS method.

## ■ ASSOCIATED CONTENT

### 📄 Supporting Information

Details of sample preparation, characterization by electron microscopy, small-angle X-ray scattering, model fitting and Porod analysis of electrodes, contrast match estimate, and illustration of direct electrode subtraction. This material is available free of charge via the Internet <http://pubs.acs.org>

## ■ AUTHOR INFORMATION

## Corresponding Author

\*E-mail: vprabhu@nist.gov. Tel. (301) 975-3657. Fax (301) 975-3928.

## Notes

The authors declare no competing financial interest.

## ■ ACKNOWLEDGMENTS

This work utilized the Center for High Resolution Neutron Scattering (CHRNS) facilities supported in part by the National Science Foundation under agreement no. DMR-0944772.

Official contribution of the National Institute of Standards and Technology; not subject to copyright in the United States

Certain commercial equipment and materials are identified in this paper to specify adequately the experimental procedure. In no case does such identification imply recommendations by the National Institute of Standards and Technology, nor does it imply that the material or equipment identified is necessarily the best available for this purpose.

## ■ REFERENCES

- (1) Auffan, M.; Rose, J.; Wiesner, M. R.; Bottero, J. Y. Chemical Stability of Metallic Nanoparticles: A Parameter Controlling their Potential Cellular Toxicity in Vitro. *Environ. Pollut.* **2009**, *157*, 1127–1133.
- (2) Puzyn, T.; Rasulev, B.; Gajewicz, A.; Hu, X. K.; Dasari, T. P.; Michalkova, A.; Hwang, H. M.; Toropov, A.; Leszczynska, D.; Leszczynski, J. Using nano-QSAR to Predict the Cytotoxicity of Metal Oxide Nanoparticles. *Nat. Nanotechnol.* **2011**, *6*, 175–178.
- (3) Li, N.; Sioutas, C.; Cho, A.; Schmitz, D.; Misra, C.; Sempf, J.; Wang, M. Y.; Oberley, T.; Froines, J.; Nel, A. Ultrafine Particulate Pollutants Induce Oxidative Stress and Mitochondrial Damage. *Environ. Health Perspect.* **2003**, *111*, 455–460.
- (4) Murray, A. R.; Kisin, E.; Leonard, S. S.; Young, S. H.; Kommineni, C.; Kagan, V. E.; Castranova, V.; Shvedova, A. A. Oxidative Stress and Inflammatory Response in Dermal Toxicity of Single-Walled Carbon Nanotubes. *Toxicology* **2009**, *257*, 161–171.
- (5) Memming, R. *Semiconductor Electrochemistry*; Wiley-VCH Verlag: Weinheim, Germany, 2001.
- (6) Reipa, V.; Holden, M. J.; Vilker, V. L. Association and Redox Properties of the Putidaredoxin Reductase-Nicotinamide Adenine Dinucleotide Complex. *Biochemistry* **2007**, *46*, 13235–13244.
- (7) Kaim, W.; Fiedler, J. Spectroelectrochemistry: the Best of Two Worlds. *Chem. Soc. Rev.* **2009**, *38*, 3373–3382.
- (8) Cabot, A.; Puentes, V. F.; Shevchenko, E.; Yin, Y.; Balcells, L.; Marcus, M. A.; Hughes, S. M.; Alivisatos, A. P. Vacancy Coalescence during Oxidation of Iron Nanoparticles. *J. Am. Chem. Soc.* **2007**, *129*, 10358.
- (9) Zheng, H. M.; Smith, R. K.; Jun, Y. W.; Kisielowski, C.; Dahmen, U.; Alivisatos, A. P. Observation of Single Colloidal Platinum Nanocrystal Growth Trajectories. *Science* **2009**, *324*, 1309–1312.
- (10) Strunz, P.; Mukherji, D.; Pigozzi, G.; Gilles, R.; Geue, T.; Pranzas, K. Characterization of Core-Shell Nanoparticles by Small Angle Neutron Scattering. *Appl. Phys. A: Mater. Sci. Process.* **2007**, *88*, 277–284.
- (11) Corcoran, S. G.; Wiesler, D. G.; Sieradzki, K. An in Situ Small Angle Neutron Scattering Investigation of Ag<sub>0.7</sub>Au<sub>0.3</sub> Dealloying under Potential Control. *Mater. Res. Soc. Symp. Proc.* **1997**, *451*, 93–98.
- (12) Kline, S. R. Reduction and Analysis of SANS and USANS Data Using IGOR Pro. *J. Appl. Crystallogr.* **2006**, *39*, 895–900.
- (13) Domenech, J.; Prieto, A. Stability of ZnO Particles in Aqueous Suspensions Under UV Illumination. *J. Phys. Chem.* **1986**, *90*, 1123–1126.
- (14) Gupta, A.; Harrison, I. R. Small-Angle X-Ray-Scattering (SAXS) in Carbonized Phenolic Resins. *Carbon* **1994**, *32*, 953–960.
- (15) Perret, R.; Ruland, W. X-Ray Small-Angle Scattering of Glassy Carbon. *J. Appl. Crystallogr.* **1972**, *5*, 183.
- (16) Russell, T. P.; Lin, J. S.; Spooner, S.; Wignall, G. D. Intercalibration of Small-Angle X-Ray and Neutron-Scattering Data. *J. Appl. Crystallogr.* **1988**, *21*, 629–638.
- (17) George, S.; Pokhrel, S.; Xia, T.; Gilbert, B.; Ji, Z. X.; Schowalter, M.; Rosenauer, A.; Damoiseaux, R.; Bradley, K. A.; Madler, L.; Nel, A. E. Use of a Rapid Cytotoxicity Screening Approach To Engineer a Safer Zinc Oxide Nanoparticle through Iron Doping. *ACS Nano* **2010**, *4*, 15–29.
- (18) Burello, E.; Worth, A. P. A Theoretical Framework for Predicting the Oxidative Stress Potential of Oxide Nanoparticles. *Nanotoxicity* **2011**, *5*, 228–235.
- (19) Moos, P. J.; Chung, K.; Woessner, D.; Honegger, M.; Cutler, N. S.; Veranth, J. M. ZnO Particulate Matter Requires Cell Contact for Toxicity in Human Colon Cancer Cells. *Chem. Res. Toxicol.* **2010**, *23*, 733–739.
- (20) Ostrovsky, S.; Kazimirsky, G.; Gedanken, A.; Brodie, C. Selective Cytotoxic Effect of ZnO Nanoparticles on Glioma Cells. *Nano Res.* **2009**, *2*, 882–890.
- (21) Nel, A. E.; Madler, L.; Velegol, D.; Xia, T.; Hoek, E. M. V.; Somasundaran, P.; Klaessig, F.; Castranova, V.; Thompson, M. Understanding Biophysicochemical Interactions at the Nano-Bio Interface. *Nat. Mater.* **2009**, *8*, 543–557.
- (22) Borm, P.; Klaessig, F. C.; Landry, T. D.; Moudgil, B.; Pauluhn, J.; Thomas, K.; Trottier, R.; Wood, S. Research Strategies for Safety Evaluation of Nanomaterials, Part V: Role of Dissolution in Biological Fate and Effects of Nanoscale Particles. *Toxicol. Sci.* **2006**, *90*, 23–32.
- (23) Nyffenegger, R. M.; Craft, B.; Shaaban, M.; Gorer, S.; Erley, G.; Penner, R. M. A Hybrid Electrochemical/Chemical Synthesis of Zinc Oxide Nanoparticles and Optically Intrinsic Thin Films. *Chem. Mater.* **1998**, *10*, 1120–1129.
- (24) Higgins, J. S.; Benoit, H. C. *Polymers and Neutron Scattering*; Oxford University Press, Inc.: New York, 2002.
- (25) Kamada, K.; Enomoto, N.; Hojo, J. Metal Plating via Electrochemical Reduction of Oxide Layers Formed by Electrophoretic Deposition. *J. Ceram. Soc. Jpn.* **2009**, *117*, 926–928.
- (26) Hoyer, P.; Weller, H. Size-Dependent Redox Potentials of Quantized Zinc-Oxide Measured with An Optically Transparent Thin-Layer Electrode. *Chem. Phys. Lett.* **1994**, *221*, 379–384.
- (27) Xiong, W.; Li, S. S. Low-Energy Exciton States in a ZnO Cylindrical Nanodisk. *J. App. Phys.* **2008**, *104*, 094310.
- (28) Haase, M.; Weller, H.; Henglein, A. Photochemistry and Radiation-Chemistry of Colloidal Semiconductors 0.23. Electron Storage on ZnO Particles and Size Quantization. *J. Phys. Chem.* **1988**, *92*, 482–487.